

Dijet production in neutral current deep inelastic scattering at HERA

ZEUS Collaboration

Abstract

Dijet cross sections in neutral current deep inelastic ep scattering have been measured in the range $10 < Q^2 < 10^4 \text{ GeV}^2$ with the ZEUS detector at HERA using an integrated luminosity of 38.4 pb^{-1} . The cross sections, measured in the Breit frame using the k_T jet algorithm, are compared with next-to-leading-order perturbative QCD calculations using proton parton distribution functions. The uncertainties of the QCD calculations have been studied. The predictions are in reasonable agreement with the measured cross sections over the entire kinematic range.

1 Introduction

Dijet production in deep inelastic ep scattering (DIS) provides a test of perturbative Quantum Chromodynamics (pQCD) and is sensitive to the structure of the proton. A comparison of measurements of dijet cross sections and pQCD predictions tests the validity of the concept of factorisation [1] into a hard partonic cross section and universal parton distribution functions (PDFs). The large centre-of-mass energy of the HERA ep collider ($\sqrt{s} \approx 300$ GeV) permits measurements of cross sections [2, 3], for jets of high transverse energy, covering over three orders of magnitude in both the photon virtuality, Q^2 , and the fraction of the proton's momentum carried by the struck parton, x .

In leading-order (LO) QCD, two processes contribute to dijet production in DIS: the QCD-Compton (QCDC) and the boson-gluon fusion (BGF) processes, shown in Figs. 1(a) and (b), respectively. The QCDC and the BGF cross sections are calculated in pQCD by convoluting the matrix element for the hard process, which depends upon the value of the QCD strong coupling constant, α_s , with the PDFs of the proton. In the high- Q^2 region, the QCDC process is dominant and the quark PDFs are well constrained by inclusive DIS data. Hence the dijet cross-section measurements allow tests of pQCD and a measurement of α_s . The extraction of α_s from the high- Q^2 dijet data and its evolution with Q^2 are the subjects of a separate publication [4]. The BGF process is the dominant contribution to dijet production at $Q^2 \lesssim 500$ GeV². Therefore, measurements of the dijet cross section at low Q^2 are sensitive to the gluon momentum distribution in the proton, $xg(x)$, at low x . The dijet cross section can be compared to the predictions of NLO QCD calculated using various parametrisations of the proton PDFs. These comparisons complement analyses that determine $xg(x)$ from the scaling violations of the structure functions [5, 6].

In this paper, the value of $\alpha_s(M_Z)$ is fixed and the inclusive dijet data (≥ 2 jets) are used to test pQCD and the universality of the proton PDFs, in particular the gluon distribution. The precision of the next-to-leading-order (NLO) QCD calculations plays an important role in this analysis and is also studied here in detail. The high-statistics dijet sample, together with improved NLO QCD calculations and a better understanding of jet-finding algorithms, permit higher-precision tests over a wider range of Q^2 , $10 < Q^2 < 10^4$ GeV², than in previous publications [2].

2 Theoretical framework

Within the framework of pQCD in DIS, the dijet production cross section, $d\sigma$, can be written as a convolution of the proton PDFs, f_a , with the partonic hard cross section, $d\hat{\sigma}_a$:

$$d\sigma = \sum_{a=q,\bar{q},g} \int dx f_a(x, \mu_F^2) d\hat{\sigma}_a(x, \alpha_s(\mu_R), \mu_R^2, \mu_F^2) \cdot (1 + \delta_{\text{had}}). \quad (1)$$

The partonic cross section describes the short-distance structure of the interaction and is calculable as a power-series expansion in the strong coupling constant. As can be seen in

Eq. (1), the cross section depends on the renormalisation scale, μ_R , since the calculations are not carried out to all orders. The PDFs contain the description of the long-distance structure of the incoming proton. The evolution of the PDFs with the factorisation scale, μ_F , at which they are determined follows the DGLAP equations [7]. The hadronisation correction, δ_{had} , can be estimated using Monte Carlo models for fragmentation (see Sections 6 and 7.2).

The predictions of QCD were calculated at NLO in α_s using the programs MEPJET [8] and DISENT [9]. These programs yield parton-level cross sections and allow for an arbitrary jet-definition scheme with user-defined cross-section cuts. Unless otherwise stated, all the pQCD predictions presented in this publication were calculated using the CTEQ4M [10] proton PDFs. The value, $\alpha_s(M_Z) = 0.116$, and the formula for the running of α_s used in MEPJET and DISENT were the same as those used in the proton PDF determination. According to calculations using DISENT, the percentage of gluon-initiated dijet events in the total dijet cross section increases from $\sim 10\%$ to $\sim 70\%$ as Q^2 decreases from 10^4 to 10 GeV².

In all NLO QCD calculations, μ_F^2 was set to Q^2 . The dependence of the pQCD predictions on μ_F^2 and μ_R^2 is discussed in Section 7.1. In DIS dijet events, there are two “natural” variables to define μ_R^2 : the Q^2 of the event and the square of the transverse energy of the event or jets. In principle, any multiple of these variables or any combination of them can be used. The interplay between these two variables has been investigated by measuring the dependence of the dijet cross section on the ratio \bar{E}_T^2/Q^2 , where \bar{E}_T is the average transverse energy of the two jets with highest transverse energy in the event.

3 Experimental setup

The dijet data sample presented here was collected with the ZEUS detector during 1996 and 1997 and corresponds to an integrated luminosity of 38.4 ± 0.6 pb⁻¹. During this period, HERA operated with protons of energy $E_p = 820$ GeV and positrons of energy $E_e = 27.5$ GeV.

The ZEUS detector is described in detail elsewhere [11, 12]. The main components used in the present analysis are the uranium-scintillator sampling calorimeter (CAL) [13], and the central tracking chamber (CTD) [14] positioned in a 1.43 T solenoidal magnetic field. The smallest subdivision of the CAL is called a cell. The CAL relative energy resolutions, as measured in test beams, are $18\%/\sqrt{E(\text{GeV})}$ and $35\%/\sqrt{E(\text{GeV})}$ for electrons and hadrons, respectively. The interaction vertex is measured using the CTD with a typical resolution along (transverse to) the beam direction¹ of 0.4 (0.1) cm.

The luminosity was measured using the Bethe-Heitler reaction $e^+p \rightarrow e^+\gamma p$ [15]. The resulting small-angle energetic photons were measured by the luminosity monitor, a lead-scintillator calorimeter placed in the HERA tunnel at $Z = -107$ m.

¹The ZEUS coordinate system is a right-handed Cartesian system, with the Z axis pointing in the proton beam direction, referred to as the “forward direction”, and the X axis pointing left towards the centre of HERA. The coordinate origin is at the nominal interaction point. The pseudorapidity is defined as $\eta = -\ln(\tan \frac{\theta}{2})$, where the polar angle, θ , is measured with respect to the proton beam direction.

4 Reconstruction of kinematic variables

The reaction

$$e^+(k) + p(P) \rightarrow e^+(k') + X$$

at fixed squared centre-of-mass energy, $s = (k + P)^2$, can be fully specified in terms of $Q^2 \equiv -q^2 = -(k - k')^2$ and Bjorken $x = Q^2/(2P \cdot q)$. The fraction of the positron's energy transferred to the proton in its rest frame is $y = Q^2/(sx)$.

For processes where two or more jets are produced in the final state, the observable ξ is defined as

$$\xi = x \left(1 + \frac{M_{JJ}^2}{Q^2} \right),$$

where the dijet mass, $M_{JJ} = \sqrt{2E_1E_2(1 - \cos\theta_{12})}$, is calculated from the energies E_1 and E_2 and the opening angle θ_{12} of the two jets of highest transverse energy. The variable ξ is the fraction of the proton momentum carried by the struck parton in the LO QCD processes (see Fig. 1).

The kinematic variables were reconstructed using a combination of the electron and the double-angle (DA) methods [16]. The electron method was used except when the angle of the hadronic system, γ_h , was less than 90° and the scattered-positron track could be well reconstructed by the CTD. In this case, the DA method was used.

The variable $y_{JB} = \sum_i E_i(1 - \cos\theta_i)/(2E_e)$, calculated according to the Jacquet-Blondel method [17], where the sum runs over all CAL cells except those belonging to the scattered positron, gives a measurement of y with good resolution at low y .

5 Selection of the dijet event sample

The events were selected online via a three-level trigger system [12, 18, 19] using the same selection algorithms as in previous dijet publications [20]. Neutral current DIS events were selected by requiring that the scattered positron was measured in the CAL [21]. Further criteria were applied both to ensure an accurate reconstruction of the kinematic variables and to increase the purity of the sample:

- $E'_e > 10$ GeV, where E'_e is the scattered positron energy, after correction for energy loss in inactive material in front of the CAL, to achieve a high-purity sample of DIS events;
- $38 \leq E - p_Z \leq 65$ GeV, where $E - p_Z = \sum_i E_i(1 - \cos\theta_i)$ and the summation is over all CAL cells, to remove background from photoproduction and events with large initial-state QED radiation;

- $y_e \leq 0.95$, where $y_e = 1 - \frac{E'_e}{2E_e}(1 - \cos\theta'_e)$ and θ'_e is the polar angle of the scattered positron. Along with the previous requirements, this reduces the photoproduction background to a negligible level [22];
- $|X| > 14$ cm or $|Y| > 14$ cm, where X and Y are the impact positions of the positron on the CAL, to avoid the low-acceptance region adjacent to the rear beampipe;
- $|Z_{\text{vertex}}| < 50$ cm, to ensure that event quantities can be accurately determined;
- $y_{JB} \geq 0.04$, to give sufficient accuracy for DA reconstruction of Q^2 and x ;
- $10 < Q^2 < 10^4$ GeV².

After these cuts, jets were reconstructed using the longitudinally invariant k_T cluster algorithm [23] in the inclusive mode. The jet search was conducted in the Breit frame [24], defined by $\mathbf{q} + 2x\mathbf{P} = 0$, where \mathbf{q} and \mathbf{P} are the three-momentum vectors of the exchanged boson and the proton, respectively. In the Breit frame, the three-momentum vectors of the exchanged boson and the incoming and outgoing partons all lie on the Z axis for a quark-parton-model type of event, i.e. the production of a single quark in the final state. For a typical QCDC or BGF event, the transverse energy in this frame is non-zero. The vector required to boost to the Breit frame was determined using the reconstructed event kinematics.

For each event, the jet search was performed over all the CAL energy deposits, considered as massless objects and boosted to the Breit frame, excluding those corresponding to the identified scattered positron candidate. The jet transverse energies were corrected for energy loss in the inactive material in front of the CAL. Events with two or more jets found in the Breit frame were selected by requiring that the two jets with the highest transverse energy satisfied the following cuts:

- $E_{T,1}^{\text{BRE}} > 8$ GeV and $E_{T,2}^{\text{BRE}} > 5$ GeV, where $E_{T,1}^{\text{BRE}}$ and $E_{T,2}^{\text{BRE}}$ are the transverse energies in the Breit frame;
- $E_{T,1}^{\text{LAB}} > 5$ GeV and $E_{T,2}^{\text{LAB}} > 5$ GeV, where $E_{T,1}^{\text{LAB}}$ and $E_{T,2}^{\text{LAB}}$ are the transverse energies of the two jets in the laboratory frame;
- $|\eta_{1,2}^{\text{LAB}}| < 2$, where $\eta_{1,2}^{\text{LAB}}$ are the pseudorapidities of the two jets in the laboratory frame.

The jet transverse energy and pseudorapidity cuts in the laboratory frame were imposed in order to select well-measured jets within the acceptance of the CAL. After all cuts, 39576 events with two or more jets, including 3902 events with three or more jets, remained in the sample.

6 Monte Carlo simulation

Monte Carlo (MC) simulations were used to correct the data for detector acceptance and resolution. Two MC models were used to generate DIS events: ARIADNE 4.10 [25] and LEPTO 6.5 [26]. In ARIADNE, the QCD cascade is simulated using the colour-dipole model. LEPTO uses the exact matrix elements to generate the hard process and the parton-shower model to simulate higher-order processes. Both models use the Lund string-fragmentation model [27] for hadronisation, as implemented in JETSET 7.4 [28]. To take into account first-order electroweak corrections, LEPTO and ARIADNE were interfaced with HERACLES 4.5.2 [29] using the DJANGO6 2.4 [30] program. The CTEQ4D proton PDFs were used. To estimate the uncertainty due to hadronisation, events were also produced using the HERWIG 5.9 generator [31], in which the fragmentation is simulated using a cluster model [32].

The ZEUS detector response was simulated with a program based on GEANT 3.13 [33]. The generated events were passed through the simulated detector, subjected to the same trigger requirements as the data and processed by the same reconstruction and offline programs.

Figures 2 and 3 show normalised uncorrected differential distributions of dijet events together with the predictions of the ARIADNE and LEPTO MC programs. As shown in Fig. 2(a), (b) and (d), the global event variables are better described by ARIADNE, while both ARIADNE and LEPTO give an adequate description of the data in Fig. 2(c). For the jet quantities, LEPTO gives a better description of the data in Fig. 3(a), while for the three other distributions, ARIADNE is better overall. Therefore, ARIADNE was used as the default MC simulation to determine the corrections from the detector to the hadron level.

7 Theoretical uncertainties

7.1 Uncertainties due to the renormalisation and factorisation scales

A study of the uncertainties introduced in the theoretical predictions from the renormalisation scale has been performed by choosing μ_R^2 to be either Q^2 or $E_T^2/4$, where E_T^2 is the square of the sum of the transverse energies of all final-state partons, and by varying each by a factor of four.

The ratio of the predicted dijet cross sections, $\sigma(\mu_R^2 = Q^2/4)/\sigma(\mu_R^2 = Q^2)$, as a function of Q^2 and $E_T^2/4$ calculated using DISSENT is shown in Fig. 4(a). The theoretical uncertainty depends mainly on Q^2 and decreases from values of about 50% at low Q^2 to about 10% at high Q^2 . The ratio of the predicted dijet cross sections, $\sigma(\mu_R^2 = E_T^2/16)/\sigma(\mu_R^2 = E_T^2/4)$, as a function of Q^2 and $E_T^2/4$ calculated using DISSENT is shown in Fig. 4(b). The estimated theoretical uncertainty observed in Fig. 4(b) is always less than that shown in Fig. 4(a) and has a similar dependence on both Q^2 and $E_T^2/4$ over the entire kinematic

range. Results similar to those shown in Fig. 4 were obtained when calculating the ratios $\sigma(\mu_R^2 = 4Q^2)/\sigma(\mu_R^2 = Q^2)$ and $\sigma(\mu_R^2 = E_T^2)/\sigma(\mu_R^2 = E_T^2/4)$. Even for E_T as high as 100 GeV, the scale uncertainty of the pQCD calculations is smaller than 10% only for Q^2 greater than 2000 GeV².

The uncertainties introduced in the theoretical predictions from the factorisation scale were studied by changing the value of $\mu_F^2 = Q^2$ by a factor of four. The resulting change in the cross section was about 5%, significantly less than when μ_R^2 was varied by the same factor.

7.2 Hadronisation uncertainty

The results of the NLO QCD programs for calculating dijet production are given in terms of jets of partons, while the measured cross sections refer to jets of hadrons. In both cases, the jets were reconstructed using the longitudinally invariant k_T algorithm in its inclusive mode. Therefore, a correction was applied to the predicted parton-level cross sections to account for the effects of hadronisation. Correction factors were defined for each bin as the ratio of the parton-level to hadron-level cross sections and were calculated using the MC simulations. The predictions of NLO QCD were divided by the mean of the correction factors calculated using the ARIADNE and LEPTO MC programs. Since LEPTO with default parameters does not agree with the data as well as ARIADNE (see Fig. 2), the LEPTO sample was reweighted to agree with the Q^2 distribution of the data. After this reweighting, all other kinematic distributions were found to agree better with the data. The difference in the LEPTO correction factors before and after reweighting was negligible.

The correction factors as a function of Q^2 were found to be ~ 1.25 at low Q^2 , falling to ~ 1.15 for $Q^2 > 100$ GeV². As a function of $\log_{10} \xi$ and \bar{E}_T^2/Q^2 , the correction was in the range 1.15 – 1.30. The difference between the mean correction factor and the individual correction factors from LEPTO and ARIADNE was defined as the uncertainty of the theoretical predictions due to uncertainties in the parton-to-hadron corrections. On average, this difference is about 5%. It is largest (12%) in the range $-2.4 < \log_{10} \xi < -2.2$, while, for $Q^2 < 25$ GeV², a difference of about 10% was observed. The correction factors obtained from HERWIG, which uses a different hadronisation model than either LEPTO or ARIADNE, were also calculated and were found to deviate by typically less than 5% from the correction factors obtained with ARIADNE.

8 Data corrections and systematic uncertainties

The cross sections for jets of hadrons in bins of $\log_{10} Q^2$, $\log_{10} \xi$ and $\log_{10}(\bar{E}_T^2/Q^2)$ were obtained by applying a bin-by-bin correction to the measured dijet distributions using ARIADNE. The corrections take into account the efficiency of the trigger, the selection criteria and the purity and efficiency of the jet reconstruction. An additional MC correction was applied to the measured cross sections to account for initial- and final-state QED-radiation effects.

A detailed study of the systematic uncertainties of the measurements was performed [34, 35]. The uncertainty due to that of the jet-energy scale was studied by selecting a separate sample of DIS events with only one jet in the final state in the laboratory frame. In this sample, the transverse energy of the scattered positron, which is known to within $\pm 1\%$ [21], balanced the transverse energy of the jet. The ratio between the jet and the positron transverse energies was evaluated as a function of the jet pseudorapidity, separately for data and MC-generated events. A difference of up to $\pm 3\%$ was observed, resulting in a systematic uncertainty of about $\pm 10\%$ for the measured cross sections throughout the kinematic range. The jet-energy scale dominates all other uncertainties except at $Q^2 > 1000 \text{ GeV}^2$, where the statistical plus other systematic uncertainties become comparable.

The other systematic uncertainties originate from the residual uncertainties in the event simulation and were estimated by correcting the data using the LEPTO correction factors and by varying the cuts in both data and MC simulation by an amount equal to the resolution on the relevant quantity. The most important were:

- *use of the MC model* - using LEPTO instead of ARIADNE to evaluate the acceptance corrections resulted in an uncertainty of typically $\pm 5\%$;
- *jet-transverse-energy cuts* - $E_{T,1}^{\text{BRE}}$, $E_{T,2}^{\text{BRE}}$, $E_{T,1}^{\text{LAB}}$ and $E_{T,2}^{\text{LAB}}$ were simultaneously varied by the jet-transverse-energy resolution near the cuts, $\pm 17\%$, to account for differences between the data and the MC simulation. This resulted in an uncertainty of up to $\pm 12\%$ and typically of $\pm 4\%$;
- *jet-pseudorapidity cuts* - a change of ± 0.1 in the $\eta_{1,2}^{\text{LAB}}$ cuts imposed on the jets in the laboratory frame resulted in an uncertainty of up to $\pm 6\%$ and typically of $\pm 2\%$;
- *$E - P_Z$ cuts* - the lower $E - P_Z$ cut of 38 GeV was varied by ± 4 GeV, resulting in an uncertainty of less than $\pm 2\%$.

All the uncertainties are correlated between bins except for that due to the acceptance correction using LEPTO. Nevertheless, they have been added in quadrature when displayed in the figures and tables, with only the uncertainty due to the jet-energy scale shown separately.

9 Results and discussion

9.1 Asymmetric jet cuts for the dijet cross section

Figure 5 shows the measured and predicted inclusive dijet cross sections at the hadron level as a function of the threshold on the transverse energy of the leading jet, $E_{T,1}^{\text{BRE,cut}}$. For this study, the requirement on the jet with the highest transverse energy was relaxed and the phase space region was defined by: $10 < Q^2 < 10^4 \text{ GeV}^2$, $y > 0.04$, $E'_e > 10 \text{ GeV}$, $E_{T,1}^{\text{BRE}} > 5 \text{ GeV}$, $E_{T,2}^{\text{BRE}} > 5 \text{ GeV}$, $E_{T,1}^{\text{LAB}} > 5 \text{ GeV}$, $E_{T,2}^{\text{LAB}} > 5 \text{ GeV}$ and $|\eta_{1,2}^{\text{LAB}}| < 2$.

The NLO QCD predictions of DISSENT with $\mu_R^2 = Q^2$ exhibit an unphysical behaviour at low $E_{T,1}^{\text{BRE,cut}}$; as the $E_{T,1}^{\text{BRE}}$ threshold decreases below 6 GeV, the predicted cross section decreases, whereas the dijet cross section should increase. This occurs because, within NLO QCD near the “symmetric-cut” threshold at which $E_{T,1}^{\text{BRE,cut}} = E_{T,2}^{\text{BRE,cut}}$, the phase space for the real emission of a third parton is reduced. This results in an incomplete cancellation between the real emission and the virtual-loop corrections [36] and hence the cross section falls. As seen in Fig. 5, the predictions of DISSENT with $\mu_R^2 = Q^2$ approach the measured cross section for $E_{T,1}^{\text{BRE,cut}} \gtrsim 6.5$ GeV.

To make comparisons of the measured dijet cross sections with the NLO QCD predictions, an asymmetric cut on the jet transverse energies of $E_{T,1}^{\text{BRE}} > 8$ GeV and $E_{T,2}^{\text{BRE}} > 5$ GeV was used for all further analysis. As seen in Fig. 5, $E_{T,1}^{\text{BRE,cut}} = 8$ GeV is sufficiently far away from the unphysical region near the symmetric-cut threshold. The predictions of NLO QCD with this cut, using DISSENT with $\mu_R^2 = Q^2$, agree with the data to within 5%. This 5% difference between the predictions and the data is well within the estimated $\pm 15\%$ systematic uncertainty of the measurements.

The NLO QCD predictions using DISSENT are also shown for the choice of $\mu_R^2 = E_T^2/4$ and underestimate the measurements by 20%. Calculations were also done using MEPJET. The predictions of MEPJET agree with those of DISSENT to within 5%.

9.2 Measurements of the dijet cross sections

The measured dijet cross sections for jets of hadrons as a function of $\log_{10} Q^2$, $\log_{10}(\bar{E}_T^2/Q^2)$ and $\log_{10} \xi$ are given in Tables 1–3 and are shown in Figs. 6–9. In Fig. 6, the predictions of ARIADNE and LEPTO are compared to the data. The MC models are in general agreement with the shapes of the distributions but fail to describe the normalisation of the measured cross sections. Both models are LO and thus the uncertainties due to the choice of μ_R^2 are substantial.

The inclusive dijet differential cross section, $d\sigma/d\log_{10} Q^2$, for jets of hadrons is compared to the predictions of NLO QCD in Fig. 7(a). The measured differential cross section decreases by two orders of magnitude in the range $10 < Q^2 < 10^4$ GeV² and is well described by the predictions using $\mu_R^2 = Q^2$. To examine deviations between the measurement and the predictions, the ratio of the measured cross sections and the predictions of DISSENT using $\mu_R^2 = Q^2$ and CTEQ4M is shown in Fig. 7(b). The NLO predictions are consistent with the measurements to within 10% for the entire Q^2 range. This difference is attributed to the fact that the measured cross section includes events with two or more jets, whereas the NLO QCD calculation is limited to final states with two or three partons only². The study of inclusive dijets in this paper will permit comparison to higher-order calculations.

The measured cross sections were also compared to the predictions of DISSENT using $\mu_R^2 = E_T^2/4$. For $Q^2 > 400$ GeV², no significant difference is seen between the predictions with $\mu_R^2 = Q^2$ and with $\mu_R^2 = E_T^2/4$. For lower values of Q^2 , the predictions with $\mu_R^2 = E_T^2/4$ underestimate the measured cross sections by as much as 30%. Figure 7

²This hypothesis is supported by the fact that the exclusive dijet cross section (for two and only two jets) at high Q^2 has been shown [4] to agree to within 1% with the predictions of DISSENT using $\mu_R^2 = Q^2$.

also shows that the predictions of DISENT with $\mu_R^2 = Q^2$ using the proton PDFs from MBFIT1M [37] and those using the CTEQ4M PDFs agree equally well with the data. The NLO QCD calculations exhibit a significant uncertainty due to the choice of μ_R^2 . The scale uncertainty decreases from ${}^{+50}_{-20}\%$ at $Q^2 \approx 15 \text{ GeV}^2$ to $\pm 10\%$ at $Q^2 = 400 \text{ GeV}^2$ and $\pm 5\%$ at $Q^2 = 10^4 \text{ GeV}^2$. Only for $Q^2 > 200 \text{ GeV}^2$ are the theoretical uncertainties comparable to the systematic uncertainties of the data.

To examine the interplay of the Q and E_T scales, $d\sigma/d\log_{10}(\bar{E}_T^2/Q^2)$ is compared to the predictions of DISENT in Fig. 8. The predictions with $\mu_R^2 = Q^2$ using either CTEQ4M or MBFIT1M agree well with the data. The scale uncertainty is $\pm(15 - 20)\%$ in the region where $\bar{E}_T^2 < Q^2$ and rises to ${}^{+40}_{-20}\%$ for $\bar{E}_T^2 > Q^2$. It is noteworthy that the prediction with $\mu_R^2 = Q^2$ gives an excellent description of the data for all values of \bar{E}_T^2/Q^2 , whereas, as can be seen from Fig. 8(b), the predictions using $\mu_R^2 = E_T^2/4$ fail to describe the data for $\bar{E}_T^2 > Q^2$.

9.3 Gluon distribution of the proton

Figure 9(a) shows $d\sigma/d\log_{10} \xi$. The requirement that two jets with high transverse energy be observed in the final state suppresses the cross section in the low- ξ region. Therefore, the measured dijet cross section rises in the interval $-2.3 < \log_{10} \xi < -1.7$. For $\log_{10} \xi > -1.7$, the cross section decreases due to the decrease of the gluon and quark densities at high x .

In Fig. 9(a), the measured cross sections are compared to the predictions of NLO QCD calculated with DISENT using both $\mu_R^2 = Q^2$ and $\mu_R^2 = E_T^2/4$. The predictions with $\mu_R^2 = Q^2$ are shown for both the CTEQ4M and the MBFIT1M proton PDFs. Figure 9(b) demonstrates that the NLO QCD predictions have large theoretical uncertainties over most of the ξ region. These uncertainties arise from the sensitivity to the choice of μ_R^2 in the low- Q^2 region, as shown in Fig. 7(b). Given these uncertainties, all of the pQCD calculations shown are consistent with the data.

The measured dijet differential cross sections as a function of ξ for different Q^2 ranges are given in Tables 4 and 5 and compared to the NLO QCD predictions in Figs. 10 and 11. At low Q^2 , the uncertainty on the measurements is similar to the difference between the predictions using CTEQ4M and MBFIT1M. As Q^2 increases, the dijet cross section is limited by the kinematic and jet cuts to high ξ values. For $Q^2 > 215 \text{ GeV}^2$, all of the predictions of NLO QCD give consistent results to $\pm 5\%$, independent of the choice of μ_R^2 ($E_T^2/4$ or Q^2) or proton PDFs (CTEQ4M or MBFIT1M). The NLO renormalisation-scale uncertainty in this range decreases from 10% to 5% as Q^2 increases. Over the entire Q^2 range of these measurements, the predictions of DISENT with $\mu_R^2 = Q^2$ are in reasonable agreement with the data.

In the range $10 < Q^2 < 464 \text{ GeV}^2$, the total experimental uncertainty of the measurement ranges from $(10 - 15)\%$ and the theoretical uncertainty, due to the variation of μ_R^2 , varies from 45% to 10%. In the low- Q^2 region, the dijet sample is dominated by gluon-induced BGF events and so could, in principle, be used to determine the gluon density. However, the size of the scale uncertainties precludes a precise extraction of the

gluon density³. The agreement between the data and the DISENT calculation indicates that the parametrisations of the gluon distribution in CTEQ4M and MBFIT1M, which are determined primarily from the measurements of the proton structure function, are consistent with these dijet measurements.

10 Conclusions

Differential dijet cross sections in neutral current deep inelastic scattering have been measured in the ranges $10 < Q^2 < 10^4 \text{ GeV}^2$, $y > 0.04$, $E'_e > 10 \text{ GeV}$, $E_{T,1}^{\text{BRE}} > 8 \text{ GeV}$, $E_{T,2}^{\text{BRE}} > 5 \text{ GeV}$, $E_{T,1}^{\text{LAB}} > 5 \text{ GeV}$, $E_{T,2}^{\text{LAB}} > 5 \text{ GeV}$ and $|\eta_{1,2}^{\text{LAB}}| < 2$ using the longitudinally invariant k_T cluster algorithm in the Breit frame.

The measured cross sections were compared to next-to-leading-order QCD calculations as implemented in DISENT and MEPJET. The measured dijet cross sections fall by two orders of magnitude over the Q^2 range considered here. The NLO QCD predictions agree with the data to within 10% when the renormalisation scale μ_R is chosen to be Q . The estimated theoretical uncertainties of up to 50% for $Q^2 < 20 \text{ GeV}^2$ arise from the absence of higher-order terms, leading to a sensitivity on the choice of the renormalisation scale. Only for $Q^2 > 200 \text{ GeV}^2$ are the theoretical uncertainties comparable to the systematic uncertainties of the data. The NLO predictions agree with the measured \bar{E}_T^2/Q^2 and ξ distributions to within 10%. Again, for these distributions, the renormalisation-scale uncertainty is large; up to 40% when $\bar{E}_T^2 > Q^2$ and 50% when $\log_{10} \xi < -2$.

At low Q^2 , the uncertainty on the measurements is similar to the difference between the predictions using the CTEQ4M and MBFIT1M parametrisations of the proton PDFs. In the range $10 < Q^2 < 464 \text{ GeV}^2$, the total experimental uncertainty of the measurement ranges from (10 – 15)% and the theoretical uncertainty, due to the variation of μ_R^2 , varies from 45% to 10%. Within these uncertainties, the measurements are consistent with a QCD prediction based on a gluon distribution extracted from scaling violations of the F_2 structure function of the proton. In this sense, therefore, these measurements are consistent with a universal gluon PDF. However, the large theoretical uncertainty precludes a useful determination of the gluon PDF in the proton using the dijet data; improved calculations are needed to exploit the full potential of this data.

Acknowledgements

The design, construction and installation of the ZEUS detector have been made possible by the ingenuity and dedicated efforts of many people from inside DESY and from the home institutes who are not listed as authors. Their contributions are acknowledged with great appreciation. The experiment was made possible by the inventiveness and the diligent efforts of the HERA machine group. The strong support and encouragement of the DESY directorate have been invaluable. We would like to thank M. H. Seymour and D. Zeppenfeld for useful discussions.

³This situation is also true for exclusive dijet production.

References

- [1] J. C. Collins, D. E. Soper and G. Sterman, in *Perturbative Quantum Chromodynamics*, A. H. Mueller (ed.), World Scientific, Singapore (1989), p. 1 and references therein.
- [2] ZEUS Coll., M.Derrick et al., Phys. Lett. B 306 (1993) 158;
ZEUS Coll., M.Derrick et al., Z. Phys. C 67 (1995) 81;
ZEUS Coll., M.Derrick et al., Phys. Lett. B 363 (1995) 201.
H1 Coll., I. Abt et al., Z. Phys. C 61 (1994) 59;
H1 Coll., T. Ahmed et al., Phys. Lett. B 346 (1995) 415;
H1 Coll., S. Aid et al., Nucl. Phys. B 449 (1995) 3;
H1 Coll., C. Adloff et al., Eur. Phys. J. C 5 (1998) 625;
H1 Coll., C. Adloff et al., Eur. Phys. J. C 6 (1999) 575;
H1 Coll., C. Adloff et al., Eur. Phys. J. C 13 (2000) 415.
- [3] H1 Coll., C. Adloff et al., Eur. Phys. J. C19 (2001) 269.
- [4] ZEUS Coll., J. Breitweg et al., Phys. Lett. B 507 (2001) 70.
- [5] ZEUS Coll., J. Breitweg et al., Eur. Phys. J. C 7 (1999) 609;
ZEUS Coll., M. Derrick et al., Phys. Lett. B 345 (1995) 576.
- [6] H1 Coll., S. Aid et al., Phys. Lett. B 354 (1995) 494;
H1 Coll., C. Adloff et al., Eur. Phys. J. C21 (2001) 33.
- [7] V.N. Gribov and L.N. Lipatov, Sov. J. Nucl. Phys. 15 (1972) 438;
L.N. Lipatov, Sov. J. Nucl. Phys. 20 (1975) 94;
Yu.L. Dokshitzer, Sov. Phys. JETP 46 (1977) 641;
G. Altarelli and G. Parisi, Nucl. Phys. B 126 (1977) 298.
- [8] E. Mirkes and D. Zeppenfeld, Phys. Lett. B 380 (1996) 205.
- [9] S. Catani and M. H. Seymour, Nucl. Phys. B 485 (1997) 291;
erratum *ibid* B 510 (1997) 503.
- [10] H. L. Lai et al., Phys. Rev. D 55 (1997) 1280.
- [11] ZEUS Coll., M. Derrick et al., Phys. Lett. B 293 (1992) 465.
- [12] ZEUS Coll., “The ZEUS Detector”, Status Report 1993, U. Holm (ed.), DESY (1993) (unpublished);
available on <http://www-zeus.desy.de/bluebook/bluebook.html>.
- [13] M. Derrick et al., Nucl. Instr. and Meth. A 309 (1991) 77;
A. Andresen et al., Nucl. Instr. and Meth. A 309 (1991) 101;
A. Bernstein et al., Nucl. Instr. and Meth. A 336 (1993) 23.
- [14] N. Harnew et al., Nucl. Instr. and Meth. A 279 (1989) 290;
B. Foster et al., Nucl. Phys. B 32 (1993) 181 (Proc. Suppl.);
B. Foster et al., Nucl. Instr. and Meth. A 338 (1994) 254.

- [15] J. Andruszków et al., DESY 92-066 (1992);
ZEUS Coll., M. Derrick et al., *Z. Phys. C* 63 (1994) 391;
J. Andruszków et al., DESY 01-041 (2001).
- [16] S. Bentvelsen, J. Engelen and P. Kooijman, *Proc. Workshop on Physics at HERA*,
Volume 1, W. Buchmüller and G. Ingleman (eds.), DESY (1992), p.23; K. C. Hoeger,
ibid, p.43.
- [17] F. Jacquet and A. Blondel, in *Proc. Study for an ep Facility for Europe*, U. Amaldi
(ed.), DESY (1979), p. 391; also in preprint DESY 79/48 (1979).
- [18] ZEUS Coll., M. Derrick et al., *Z. Phys. C* 72 (1996) 47.
- [19] ZEUS Coll., J. Breitweg et al., *Z. Phys. C* 74 (1997) 207.
- [20] ZEUS Coll., J. Breitweg et al., *Phys. Lett. B* 479 (2000) 37;
ZEUS Coll., J. Breitweg et al., *Eur. Phys. J. C* 1 (1998) 109.
- [21] ZEUS Coll., J. Breitweg et al., *Eur. Phys. J. C* 11 (1999) 427.
- [22] ZEUS Coll., S. Chekanov et al., DESY 01-064, accepted by *Eur. Phys. J. C*.
- [23] S. Catani et al., *Nucl. Phys. B* 406 (1993) 187;
S.D. Ellis and D.E. Soper, *Phys. Rev. D* 48 (1993) 3160.
- [24] R.P. Feynman, *Photon-Hadron Interactions*, Benjamin, N.Y. (1972);
K.H. Streng, T.F. Walsh and P.M. Zerwas, *Z. Phys. C* 2 (1979) 237.
- [25] L. Lönnblad, *Comp. Phys. Comm.* 71 (1992) 15.
- [26] LEPTO 6.5, G. Ingelman, A. Edin and J. Rathsman, *Comp. Phys. Comm.* 101
(1997) 108.
- [27] B. Andersson et al., *Phys. Rep.* 97 (1983) 31.
- [28] T. Sjöstrand, *Comp. Phys. Comm.* 82 (1994) 74;
T. Sjöstrand, CERN-TH 7112/93 (revised August 1995).
- [29] A. Kwiatkowski, H. Spiesberger, and H.-J. Möhring, *Comp. Phys. Commun.* 69
(1992) 155;
H. Spiesberger, *HERACLES - An Event Generator for ep Interactions at
HERA Including Radiative Processes (Version 4.6)*, 1996, available on:
www.desy.de/~hspiesb/heracles.html.
- [30] K. Charchuła, G. Schuler and H. Spiesberger, *Comp. Phys. Comm.* 81 (1994) 381;
H. Spiesberger, *DJANGO6 version 2.4 - A Monte Carlo Generator for Deep Inelastic
Lepton Proton Scattering Including QED and QCD Radiative Effects*, 1996, available
on: www.desy.de/~hspiesb/django6.html.
- [31] G. Marchesini et al., *Comp. Phys. Comm.* 67 (1992) 465.
- [32] B.R. Webber, *Nucl. Phys. B* 238 (1984) 492.

- [33] R. Brun et al., GEANT3, CERN DD/EE/84-1 (1987).
- [34] M. Przybycień, PhD Thesis, Institute of Nuclear Physics, Cracow, (1999) DESY-THESIS-1999-003.
- [35] D. Chapin, PhD Thesis, University of Wisconsin, Madison (2001) (unpublished).
- [36] M. Klasen and G. Kramer, Phys. Lett. B 366 (1996) 385;
S. Frixione and G. Ridolfi, Nucl. Phys. B 507 (1997) 315;
B. Pötter, hep-ph/9911221.
- [37] M. Botje, Eur. Phys. J. C 14 (2000) 285.

$\log_{10}Q^2$ bin	$d\sigma/d\log_{10}Q^2$	Δ_{stat}	Δ_{sys}	Δ_{ES} (pb)	ISR/FSR correction
1.00, 1.20	1120.5	± 18.5	$+154.3$ -141.4	$+92.3$ -93.0	1.024 ± 0.012
1.20, 1.40	967.7	± 17.7	$+80.0$ -95.8	$+84.5$ -85.6	1.040 ± 0.014
1.40, 1.60	853.6	± 16.7	$+46.0$ -66.9	$+68.5$ -75.0	0.990 ± 0.014
1.60, 1.80	690.5	± 15.1	$+34.3$ -24.0	$+60.9$ -56.3	1.002 ± 0.016
1.80, 2.00	549.4	± 13.3	$+35.0$ -14.6	$+45.5$ -44.2	0.987 ± 0.018
2.00, 2.33	368.2	± 7.3	$+16.1$ -11.5	$+24.1$ -26.1	0.989 ± 0.012
2.33, 2.67	219.1	± 5.1	$+5.3$ -5.3	$+13.8$ -14.0	1.004 ± 0.011
2.67, 3.00	113.5	± 3.5	$+2.2$ -4.3	$+5.7$ -5.9	1.021 ± 0.012
3.00, 3.50	44.2	± 1.6	$+2.4$ -0.6	$+2.2$ -2.4	0.980 ± 0.007
3.50, 4.00	8.7	± 0.7	$+0.8$ -0.7	$+0.3$ -0.4	0.960 ± 0.008

Table 1: Dijet cross sections, $d\sigma/d\log_{10}Q^2$, where Q^2 is in GeV^2 , for jets of hadrons in the Breit frame, selected with the inclusive k_T algorithm in the ranges $10 < Q^2 < 10^4 \text{ GeV}^2$, $y > 0.04$, $E'_e > 10 \text{ GeV}$, $E_{T,1}^{\text{BRE}} > 8 \text{ GeV}$, $E_{T,2}^{\text{BRE}} > 5 \text{ GeV}$, $E_{T,1}^{\text{LAB}} > 5 \text{ GeV}$, $E_{T,2}^{\text{LAB}} > 5 \text{ GeV}$ and $|\eta_{1,2}^{\text{LAB}}| < 2$. The statistical, systematic and jet-energy-scale uncertainties are shown separately. The multiplicative correction applied to account for effects of initial- and final-state QED radiation is shown in the last column.

$\log_{10}(\bar{E}_T^2/Q^2)$ bin	$d\sigma/d\log_{10}(\bar{E}_T^2/Q^2)$	Δ_{stat}	Δ_{sys}	Δ_{ES} (pb)	ISR/FSR correction
-1.70, -1.00	27.6	± 1.1	$+1.8$ -1.2	$+0.9$ -0.6	0.943 ± 0.010
-1.00, -0.70	96.5	± 3.4	$+3.9$ -2.4	$+4.3$ -6.7	0.978 ± 0.013
-0.70, -0.30	213.2	± 5.0	$+7.5$ -5.2	$+9.4$ -11.4	1.009 ± 0.012
-0.30, +0.00	429.5	± 9.4	$+21.6$ -12.6	$+27.9$ -26.6	1.000 ± 0.014
+0.00, +0.30	640.9	± 12.2	$+30.7$ -26.7	$+46.3$ -48.8	0.994 ± 0.013
+0.30, +0.70	901.3	± 12.7	$+45.0$ -45.6	$+75.7$ -73.5	1.010 ± 0.010
+0.70, +1.00	688.7	± 12.5	$+14.6$ -30.4	$+64.7$ -67.4	1.021 ± 0.013
+1.00, +1.70	113.6	± 2.8	$+1.9$ -6.4	$+11.9$ -11.9	1.029 ± 0.017

Table 2: Dijet cross sections, $d\sigma/d\log_{10}(\bar{E}_T^2/Q^2)$, for jets of hadrons in the Breit frame, selected with the inclusive k_T algorithm. For details, see the caption of Table 1.

$\log_{10} \xi$ bin	$d\sigma/d\log_{10} \xi$	Δ_{stat}	Δ_{sys}	Δ_{ES}	ISR/FSR correction
-2.40, -2.20	198.2	± 8.1	$+13.1$ -10.4	$+26.4$ -25.6	1.138 ± 0.037
-2.20, -2.00	636.4	± 14.8	$+27.7$ -59.8	$+55.8$ -56.1	1.052 ± 0.018
-2.00, -1.80	1084.5	± 19.5	$+57.7$ -57.2	$+83.0$ -88.4	1.043 ± 0.013
-1.80, -1.60	1251.4	± 20.6	$+63.3$ -63.1	$+81.7$ -85.0	0.995 ± 0.011
-1.60, -1.40	1147.9	± 20.0	$+52.7$ -53.6	$+74.2$ -80.2	0.980 ± 0.011
-1.40, -1.20	653.7	± 15.0	$+39.8$ -24.1	$+53.4$ -42.4	0.994 ± 0.013
-1.20, -1.00	273.9	± 9.5	$+11.1$ -9.7	$+17.5$ -21.5	0.986 ± 0.019
-1.00, -0.80	82.6	± 5.0	$+3.8$ -7.0	$+6.3$ -3.9	0.997 ± 0.031

Table 3: Dijet cross sections, $d\sigma/d\log_{10} \xi$, for jets of hadrons in the Breit frame, selected with the inclusive k_T algorithm. For details, see the caption of Table 1.

$\log_{10} \xi$ bin	$d\sigma/d\log_{10} \xi$	Δ_{stat}	Δ_{sys}	Δ_{ES} (pb)	ISR/FSR correction
$1.0 < \log_{10} Q^2 < 1.2$					
-2.40, -2.20	70.2	± 4.9	$+7.0$ -3.9	$+6.6$ -7.2	1.173 ± 0.065
-2.20, -2.00	169.9	± 7.7	$+20.3$ -21.5	$+14.6$ -16.7	1.021 ± 0.034
-2.00, -1.80	261.9	± 9.9	$+25.9$ -27.8	$+21.2$ -19.9	1.073 ± 0.028
-1.80, -1.60	251.5	± 9.3	$+22.2$ -21.4	$+15.7$ -15.4	1.002 ± 0.024
-1.60, -1.40	199.6	± 8.4	$+18.8$ -21.7	$+13.9$ -16.9	1.012 ± 0.026
-1.40, -1.20	78.4	± 5.0	$+12.9$ -3.7	$+6.3$ -5.2	0.967 ± 0.034
$1.2 < \log_{10} Q^2 < 1.4$					
-2.40, -2.20	55.9	± 4.6	$+1.5$ -7.1	$+8.1$ -8.8	1.214 ± 0.077
-2.20, -2.00	142.2	± 7.2	$+13.2$ -13.5	$+14.8$ -11.3	1.092 ± 0.041
-2.00, -1.80	222.5	± 9.3	$+7.3$ -13.3	$+17.8$ -19.6	1.089 ± 0.032
-1.80, -1.60	212.8	± 8.6	$+17.0$ -10.7	$+14.9$ -10.8	1.003 ± 0.027
-1.60, -1.40	181.2	± 8.2	$+9.4$ -14.9	$+11.2$ -15.1	0.968 ± 0.028
-1.40, -1.20	83.3	± 5.6	$+15.0$ -2.2	$+6.1$ -7.1	1.108 ± 0.042
$1.4 < \log_{10} Q^2 < 1.6$					
-2.40, -2.20	33.9	± 3.2	$+3.8$ -2.4	$+5.9$ -3.2	1.084 ± 0.083
-2.20, -2.00	128.0	± 7.0	$+3.0$ -17.2	$+8.2$ -11.3	1.064 ± 0.044
-2.00, -1.80	182.7	± 8.2	$+2.9$ -8.7	$+12.9$ -16.9	0.988 ± 0.032
-1.80, -1.60	198.4	± 8.5	$+8.8$ -19.2	$+12.6$ -16.6	0.938 ± 0.028
-1.60, -1.40	165.2	± 7.9	$+11.7$ -8.6	$+13.5$ -9.6	1.000 ± 0.031
-1.40, -1.20	89.5	± 6.1	$+5.1$ -6.7	$+7.9$ -9.5	0.977 ± 0.040
$1.6 < \log_{10} Q^2 < 1.8$					
-2.40, -2.20	25.5	± 2.9	$+1.2$ -1.4	$+3.2$ -3.9	1.085 ± 0.100
-2.20, -2.00	83.0	± 5.3	$+1.7$ -7.7	$+8.7$ -7.6	1.032 ± 0.050
-2.00, -1.80	146.4	± 7.3	$+11.6$ -8.8	$+11.5$ -12.1	1.059 ± 0.038
-1.80, -1.60	172.0	± 8.0	$+21.3$ -3.9	$+13.2$ -11.2	1.000 ± 0.033
-1.60, -1.40	149.1	± 7.6	$+3.8$ -1.7	$+9.7$ -10.8	0.942 ± 0.032
-1.40, -1.20	69.2	± 5.2	$+3.5$ -6.0	$+8.4$ -3.9	0.988 ± 0.046
$1.8 < \log_{10} Q^2 < 2.0$					
-2.20, -2.00	61.6	± 4.5	$+2.6$ -5.7	$+6.5$ -4.7	1.019 ± 0.057
-2.00, -1.80	113.0	± 6.3	$+4.5$ -3.7	$+6.2$ -8.6	1.008 ± 0.041
-1.80, -1.60	133.7	± 6.9	$+8.7$ -3.3	$+12.2$ -9.6	1.019 ± 0.037
-1.60, -1.40	124.5	± 6.8	$+7.0$ -3.7	$+8.0$ -9.6	0.941 ± 0.035
-1.40, -1.20	66.8	± 5.1	$+7.2$ -5.2	$+8.1$ -5.2	0.943 ± 0.044

Table 4: Dijet cross sections, $d\sigma/d\log_{10} \xi$, for jets of hadrons in the Breit frame, selected with the inclusive k_T algorithm. For details, see the caption of Table 1.

$\log_{10} \xi$ bin	$d\sigma/d\log_{10} \xi$	Δ_{stat}	Δ_{sys}	Δ_{ES}	ISR/FSR correction
$2.0 < \log_{10} Q^2 < 2.33$					
-2.20, -2.00	43.2	± 3.2	$^{+5.3}_{-1.7}$	$^{+2.3}_{-3.2}$	1.126 ± 0.054
-2.00, -1.80	105.9	± 5.1	$^{+9.5}_{-7.0}$	$^{+8.3}_{-8.5}$	0.997 ± 0.029
-1.80, -1.60	153.2	± 6.5	$^{+3.6}_{-7.6}$	$^{+8.1}_{-11.7}$	0.980 ± 0.024
-1.60, -1.40	148.7	± 6.5	$^{+6.4}_{-3.1}$	$^{+9.3}_{-7.1}$	0.972 ± 0.023
-1.40, -1.20	94.7	± 5.4	$^{+2.2}_{-6.6}$	$^{+6.3}_{-5.8}$	0.981 ± 0.028
$2.33 < \log_{10} Q^2 < 2.67$					
-2.00, -1.80	44.2	± 3.0	$^{+2.3}_{-3.3}$	$^{+4.6}_{-2.3}$	1.030 ± 0.032
-1.80, -1.60	87.1	± 4.5	$^{+3.0}_{-1.9}$	$^{+2.5}_{-5.6}$	1.062 ± 0.024
-1.60, -1.40	104.0	± 5.1	$^{+3.9}_{-5.2}$	$^{+5.2}_{-7.6}$	0.988 ± 0.020
-1.40, -1.20	75.7	± 4.2	$^{+7.6}_{-2.4}$	$^{+5.9}_{-2.5}$	0.964 ± 0.021
-1.20, -1.00	38.1	± 3.2	$^{+3.4}_{-0.8}$	$^{+2.4}_{-3.5}$	0.979 ± 0.030
$2.67 < \log_{10} Q^2 < 3.0$					
-2.00, -1.80	6.4	± 0.9	$^{+1.0}_{-0.6}$	$^{+0.6}_{-0.4}$	1.052 ± 0.062
-1.80, -1.60	31.1	± 2.2	$^{+0.4}_{-1.2}$	$^{+1.4}_{-2.5}$	0.992 ± 0.029
-1.60, -1.40	47.5	± 2.9	$^{+3.1}_{-1.9}$	$^{+2.6}_{-2.1}$	1.010 ± 0.024
-1.40, -1.20	54.2	± 3.3	$^{+1.7}_{-4.9}$	$^{+1.6}_{-2.1}$	1.034 ± 0.024
-1.20, -1.00	33.1	± 2.6	$^{+2.7}_{-2.1}$	$^{+2.6}_{-1.9}$	1.053 ± 0.029
$3.0 < \log_{10} Q^2 < 3.5$					
-1.80, -1.60	5.2	± 0.9	$^{+1.5}_{-1.5}$	$^{+0.5}_{-0.8}$	1.060 ± 0.038
-1.60, -1.40	18.7	± 1.7	$^{+2.9}_{-1.0}$	$^{+0.6}_{-1.4}$	0.981 ± 0.018
-1.40, -1.20	32.3	± 2.3	$^{+1.3}_{-1.6}$	$^{+2.1}_{-1.5}$	0.982 ± 0.014
-1.20, -1.00	28.9	± 2.1	$^{+2.2}_{-0.6}$	$^{+1.1}_{-0.9}$	0.968 ± 0.014
-1.00, -0.80	18.6	± 1.7	$^{+0.9}_{-1.1}$	$^{+0.4}_{-0.9}$	0.969 ± 0.017
-0.80, -0.60	5.6	± 0.9	$^{+0.7}_{-0.6}$	$^{+0.7}_{-0.3}$	0.981 ± 0.032
$3.5 < \log_{10} Q^2 < 4.0$					
-1.40, -1.20	0.9	± 0.4	$^{+0.7}_{-0.0}$	$^{+0.3}_{-0.0}$	1.092 ± 0.041
-1.20, -1.00	6.4	± 1.0	$^{+0.6}_{-1.1}$	$^{+0.0}_{-0.5}$	0.981 ± 0.018
-1.00, -0.80	5.7	± 0.9	$^{+1.0}_{-0.2}$	$^{+0.3}_{-0.1}$	0.957 ± 0.014
-0.80, -0.60	6.9	± 1.0	$^{+0.3}_{-0.7}$	$^{+0.1}_{-0.3}$	0.923 ± 0.015
-0.60, -0.40	1.9	± 0.5	$^{+0.5}_{-0.4}$	$^{+0.1}_{-0.1}$	0.964 ± 0.027

Table 5: Continuation of Table 4. For details, see the caption of Table 1.

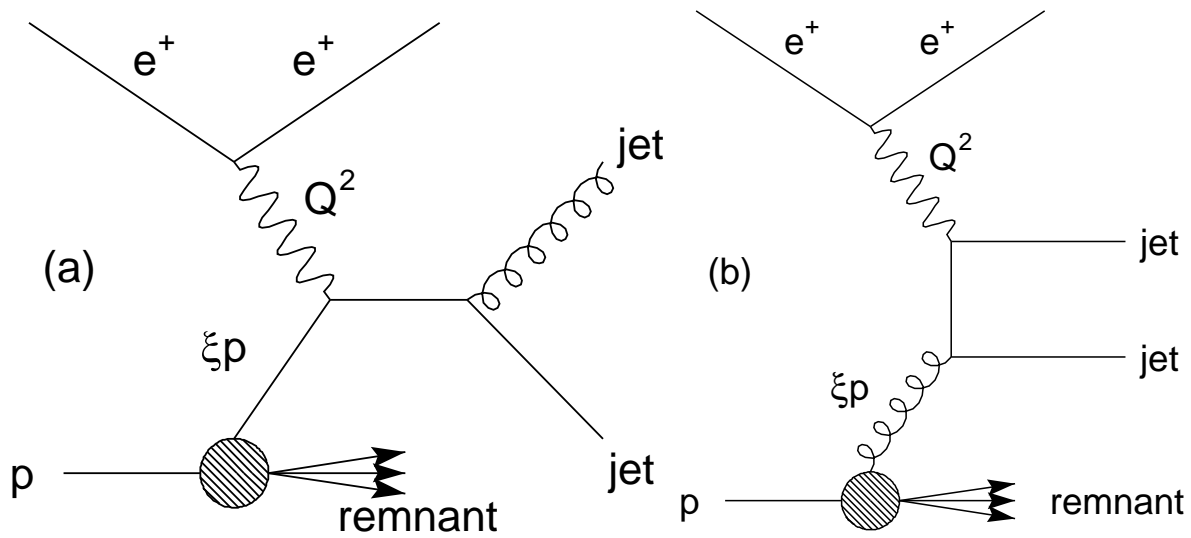


Figure 1: (a) The QCD-Compton diagram and (b) the boson-gluon fusion diagram. The fraction of the proton momentum, p , carried by the stuck parton is ξ .

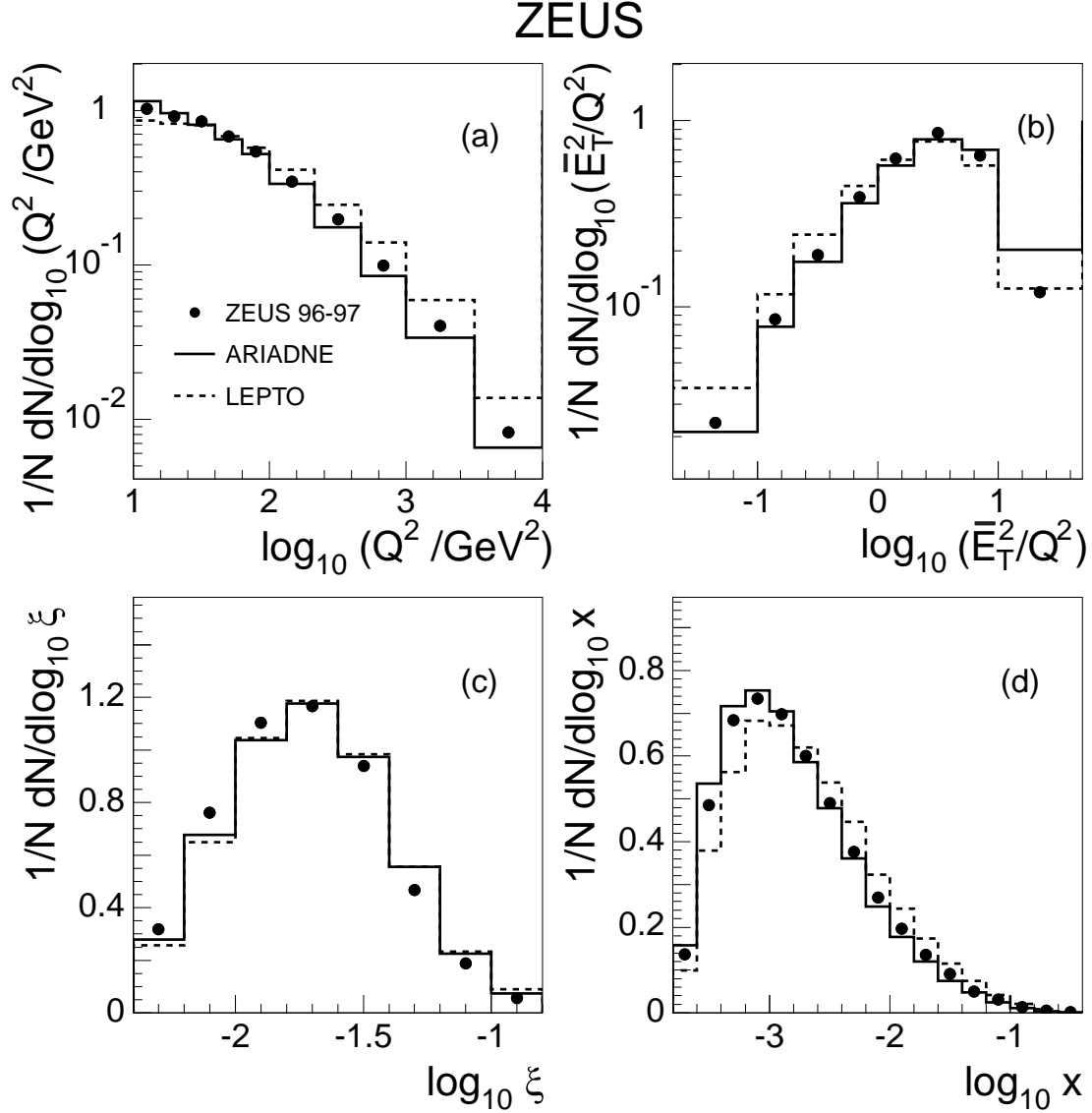


Figure 2: Normalised uncorrected distributions of (a) $\log_{10}(Q^2/\text{GeV}^2)$, (b) $\log_{10}(\bar{E}_T^2/Q^2)$, (c) $\log_{10}\xi$ and (d) $\log_{10}x$ for dijet events selected with the k_T algorithm in the Breit frame, for $E_{T,1}^{\text{BRE}} > 8 \text{ GeV}$, $E_{T,2}^{\text{BRE}} > 5 \text{ GeV}$, $E_{T,1}^{\text{LAB}} > 5 \text{ GeV}$, $E_{T,2}^{\text{LAB}} > 5 \text{ GeV}$, $|\eta_{1,2}^{\text{LAB}}| < 2$, $y > 0.04$ and $E_e' > 10 \text{ GeV}$ in the range $10 < Q^2 < 10^4 \text{ GeV}^2$. The points are the measurements. The statistical uncertainties are generally smaller than the symbols. The solid and dashed histograms are the predictions of the ARIADNE 4.10 and LEPTO 6.5 Monte Carlo programs, respectively.

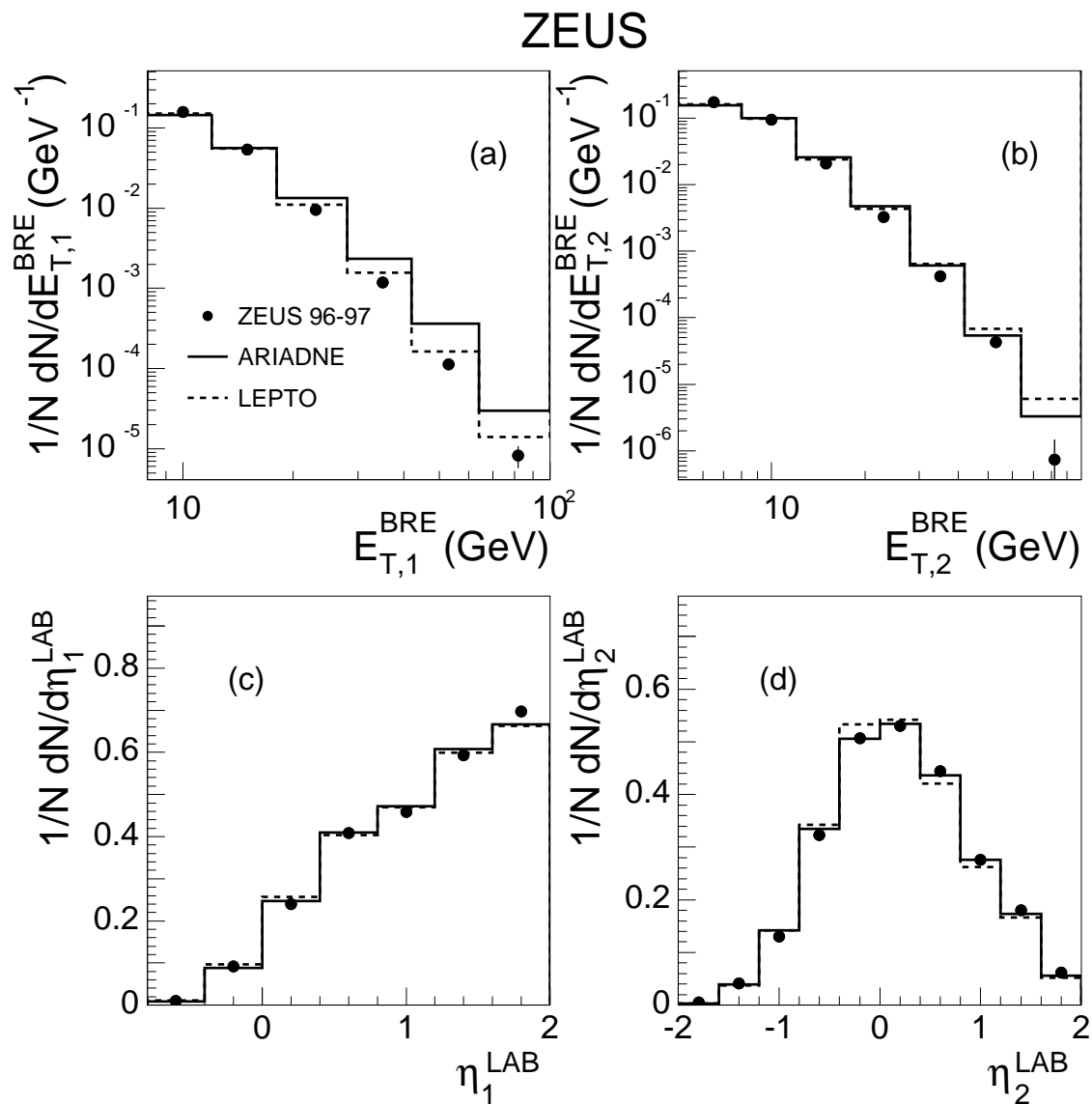


Figure 3: Normalised uncorrected distributions of (a) $E_{T,1}^{BRE}$, (b) $E_{T,2}^{BRE}$, (c) η_1^{LAB} and (d) η_2^{LAB} for dijet events selected with the k_T algorithm in the Breit frame. For details, see the caption of Fig. 2.

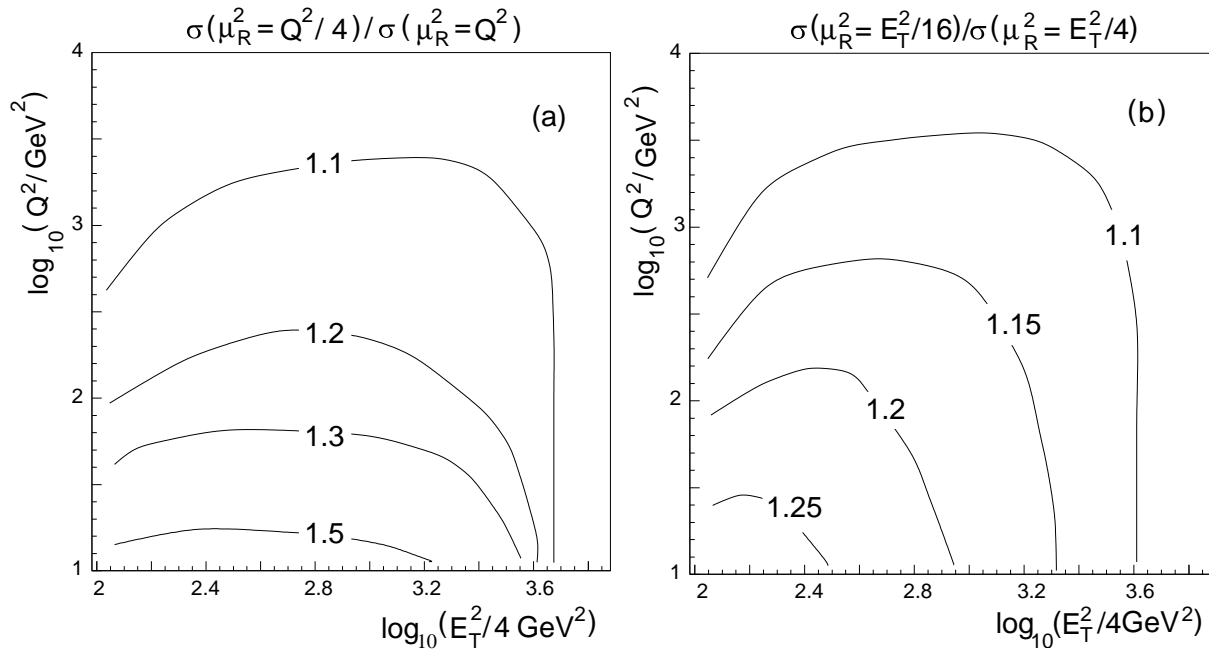


Figure 4: Contours representing a fixed scale uncertainty of the NLO QCD calculations as a function of $\log_{10} Q^2$ and $\log_{10}(E_T^2/4)$, where Q^2 and E_T^2 are in GeV^2 . The scale uncertainty shown in (a) was calculated by taking the ratio of the predicted dijet cross sections $\sigma(\mu_R^2 = Q^2/4)/\sigma(\mu_R^2 = Q^2)$; that shown in (b) was calculated by taking the ratio of the predicted dijet cross sections $\sigma(\mu_R^2 = E_T^2/16)/\sigma(\mu_R^2 = E_T^2/4)$. The cross sections were calculated using DISENT and refer to jets of partons selected with the inclusive k_T jet algorithm in the Breit frame. CTEQ4M was used for the proton PDFs.

ZEUS

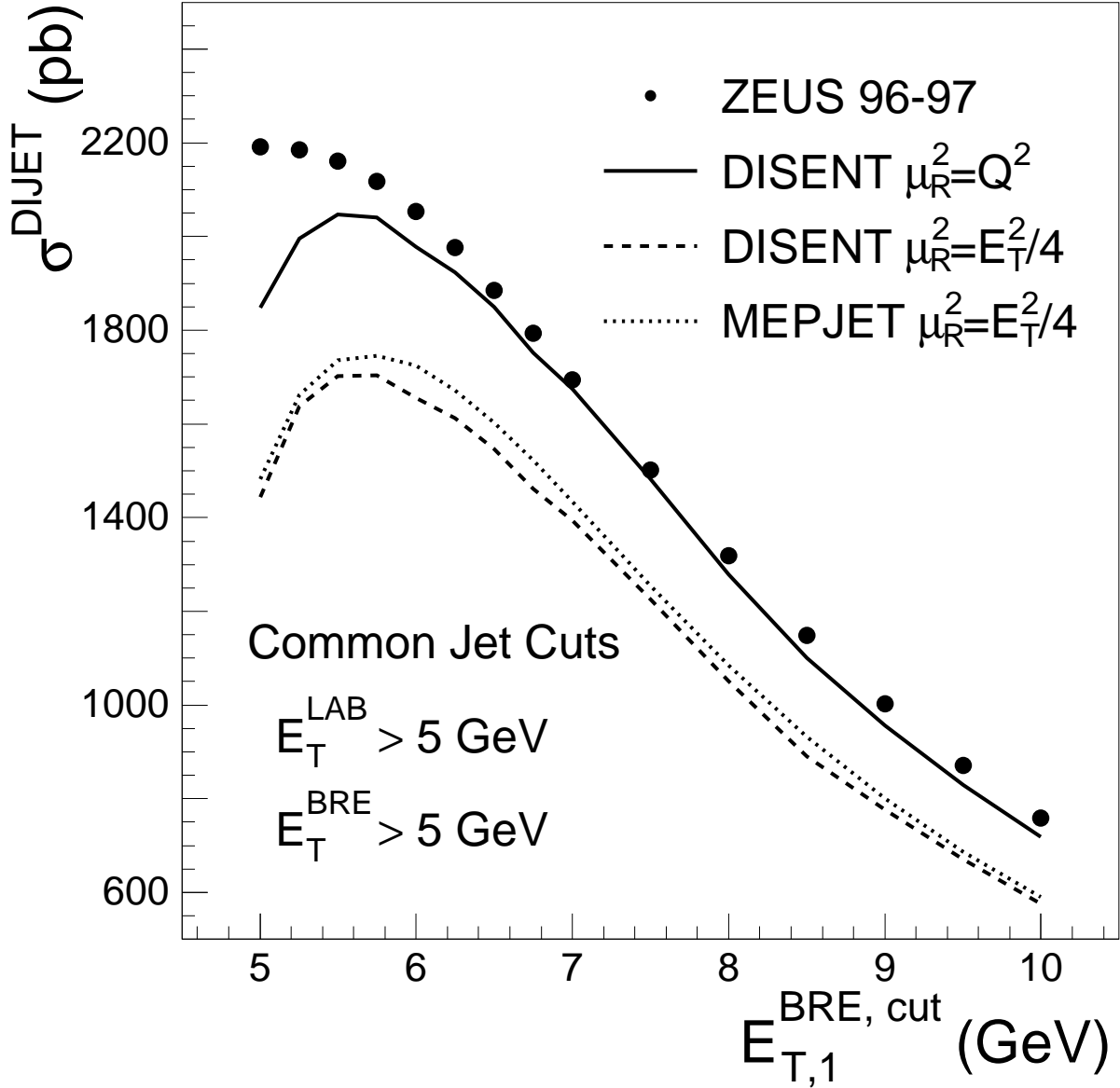


Figure 5: The dijet cross section for jets of hadrons in the Breit frame, selected with the inclusive k_T algorithm as a function of $E_{T,1}^{\text{BRE,cut}}$. The points represent the measured cross section. The typical magnitude of the statistical and systematic uncertainties added in quadrature is $\pm 15\%$. The full line represents the predictions of NLO QCD using DISSENT with $\mu_R^2 = Q^2$. The dashed line is the prediction of DISSENT with $\mu_R^2 = E_T^2/4$. The dotted line is the prediction of MEPJET with $\mu_R^2 = E_T^2/4$. All three pQCD calculations use the CTEQ4M proton PDFs, refer to jets of hadrons and were obtained by dividing the parton-level predictions of DISSENT by correction factors computed using the ARIADNE 4.10 MC simulation.

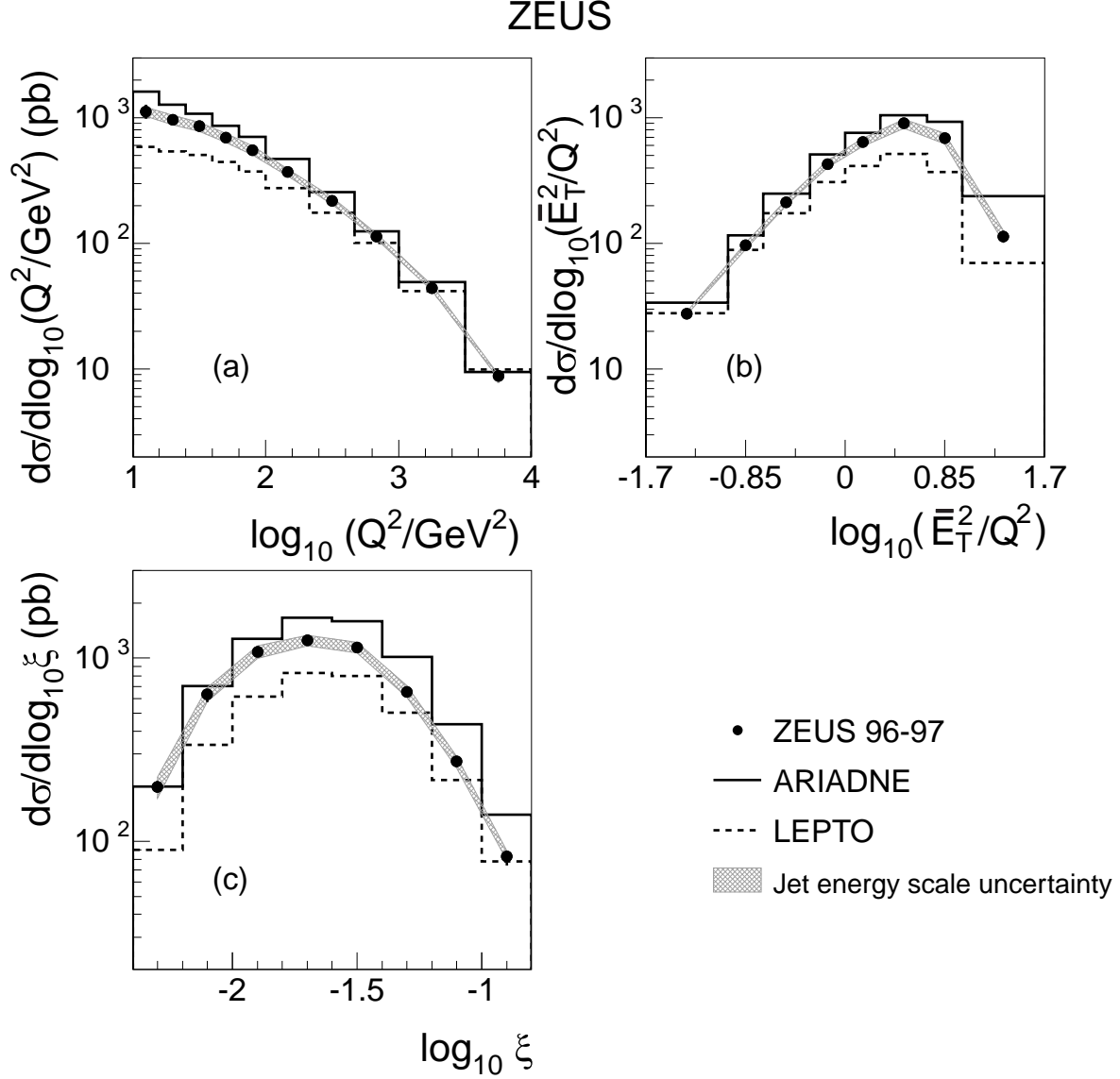


Figure 6: Dijet cross sections (a) $d\sigma/d\log_{10}(Q^2/\text{GeV}^2)$, (b) $d\sigma/d\log_{10}(\bar{E}_T^2/Q^2)$ and (c) $d\sigma/d\log_{10}\xi$ for jets of hadrons in the Breit frame selected with the inclusive k_T algorithm. The points represent the measured cross sections. The error bars are generally smaller than the points. The shaded band represents the systematic uncertainty due to the jet-energy scale. The full (dashed) histogram represents the predictions of ARIADNE 4.10 (LEPTO 6.5) with the CTEQ4M proton PDFs.

ZEUS

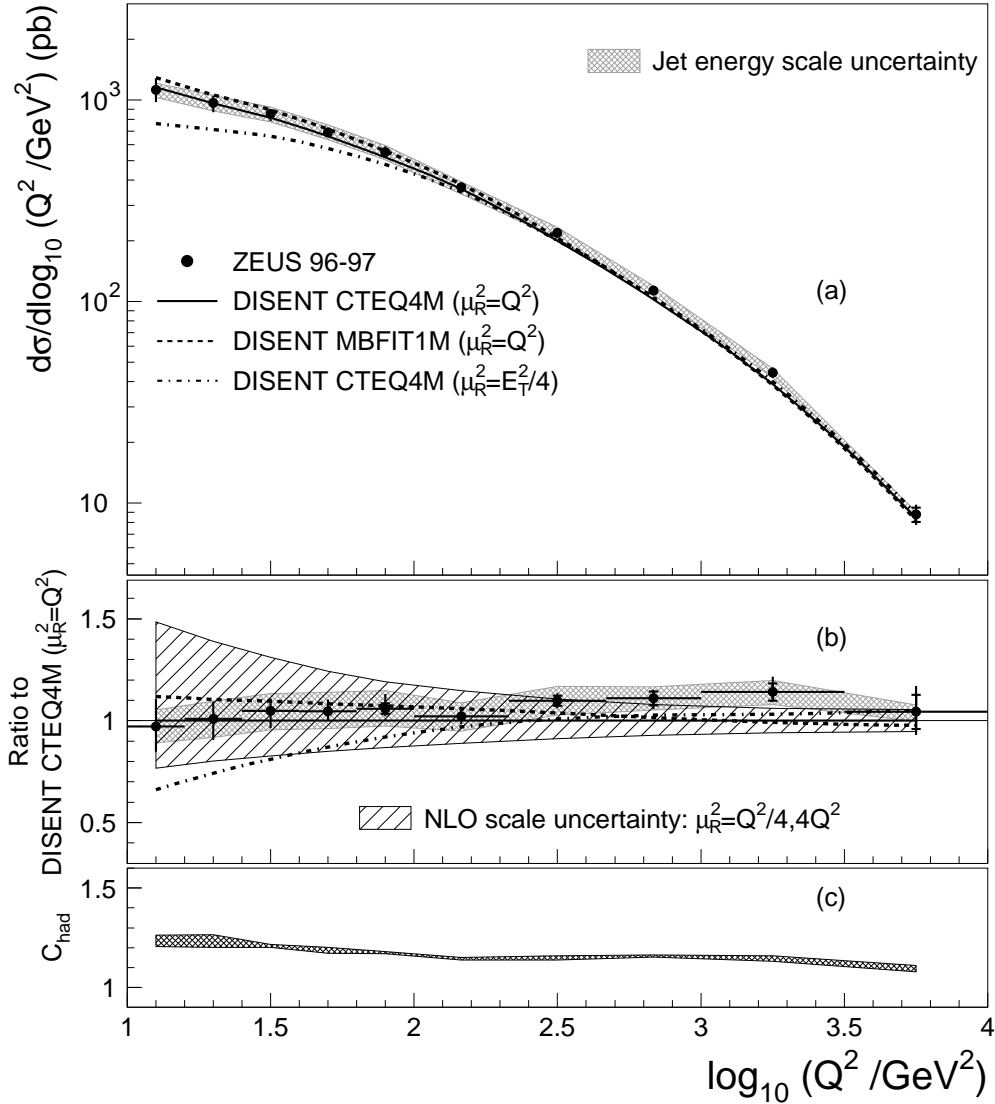


Figure 7: (a) Dijet cross section, $d\sigma/d\log_{10} Q^2$, for jets of hadrons in the Breit frame selected with the inclusive k_T algorithm. The points represent the measured cross sections. The inner error bars represent the statistical uncertainties and the outer bars are the statistical and the systematic uncertainties added in quadrature. The shaded band represents the systematic uncertainty due to the jet-energy scale. The full line represents the predictions of NLO QCD using DISSENT with $\mu_R^2 = Q^2$ and the CTEQ4M proton PDFs. The dashed-dotted line is the prediction of DISSENT with $\mu_R^2 = E_T^2/4$ and the CTEQ4M PDFs. The dashed line is the prediction of DISSENT with $\mu_R^2 = Q^2$ using the MBFIT1M proton PDFs. (b) The cross sections in (a) divided by the predictions of DISSENT with $\mu_R^2 = Q^2$ and the CTEQ4M PDFs. The cross-hatched band represents the theoretical uncertainty due to the choice of μ_R^2 calculated by choosing $\mu_R^2 = Q^2/4$ and $\mu_R^2 = Q^2$. All of the pQCD predictions shown here refer to jets of hadrons and were obtained by dividing the parton-level predictions of DISSENT by the average value of the correction factors computed using the LEPTO 6.5 and the ARIADNE 4.10 MC simulations. The shaded band in (c) shows the magnitude and the uncertainty of this parton-to-hadron correction.

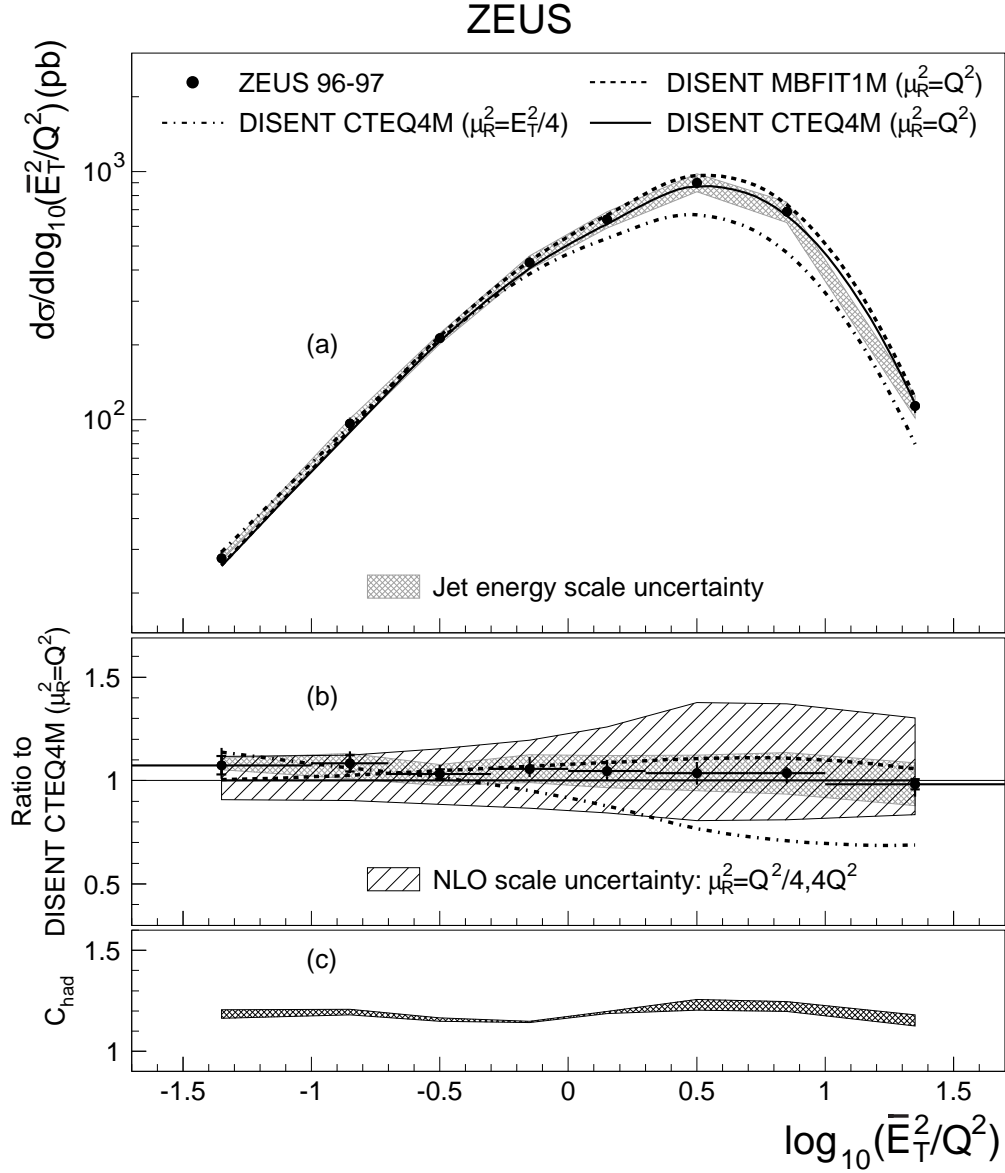


Figure 8: Dijet cross section, $d\sigma/d\log_{10}(\bar{E}_T^2/Q^2)$, for jets of hadrons in the Breit frame selected with the inclusive k_T algorithm. Other details are as described in the caption of Fig. 7.

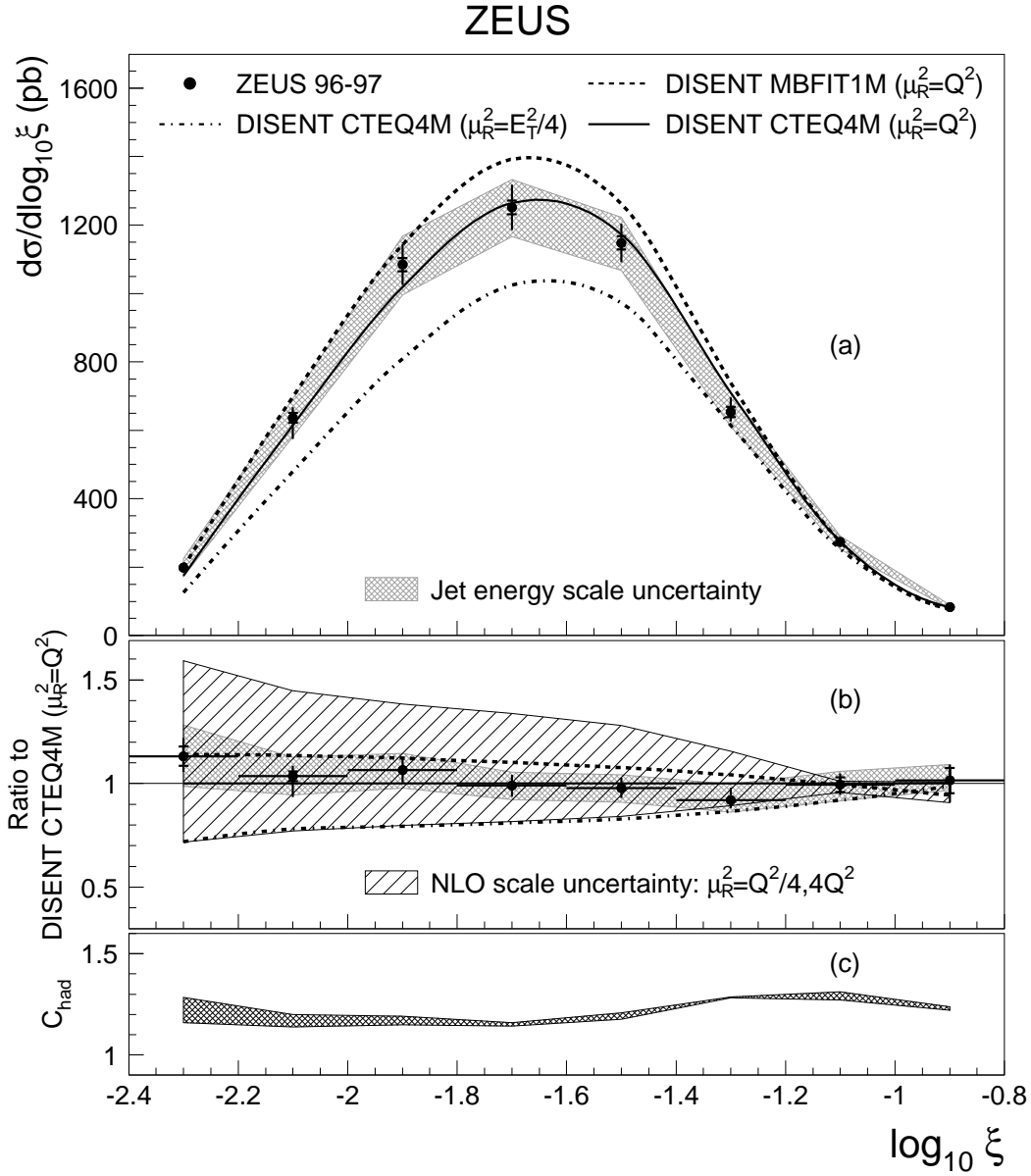


Figure 9: Dijet cross section, $d\sigma/d\log_{10} \xi$, for jets of hadrons in the Breit frame selected with the inclusive k_T algorithm. Other details are as described in the caption of Fig. 7.

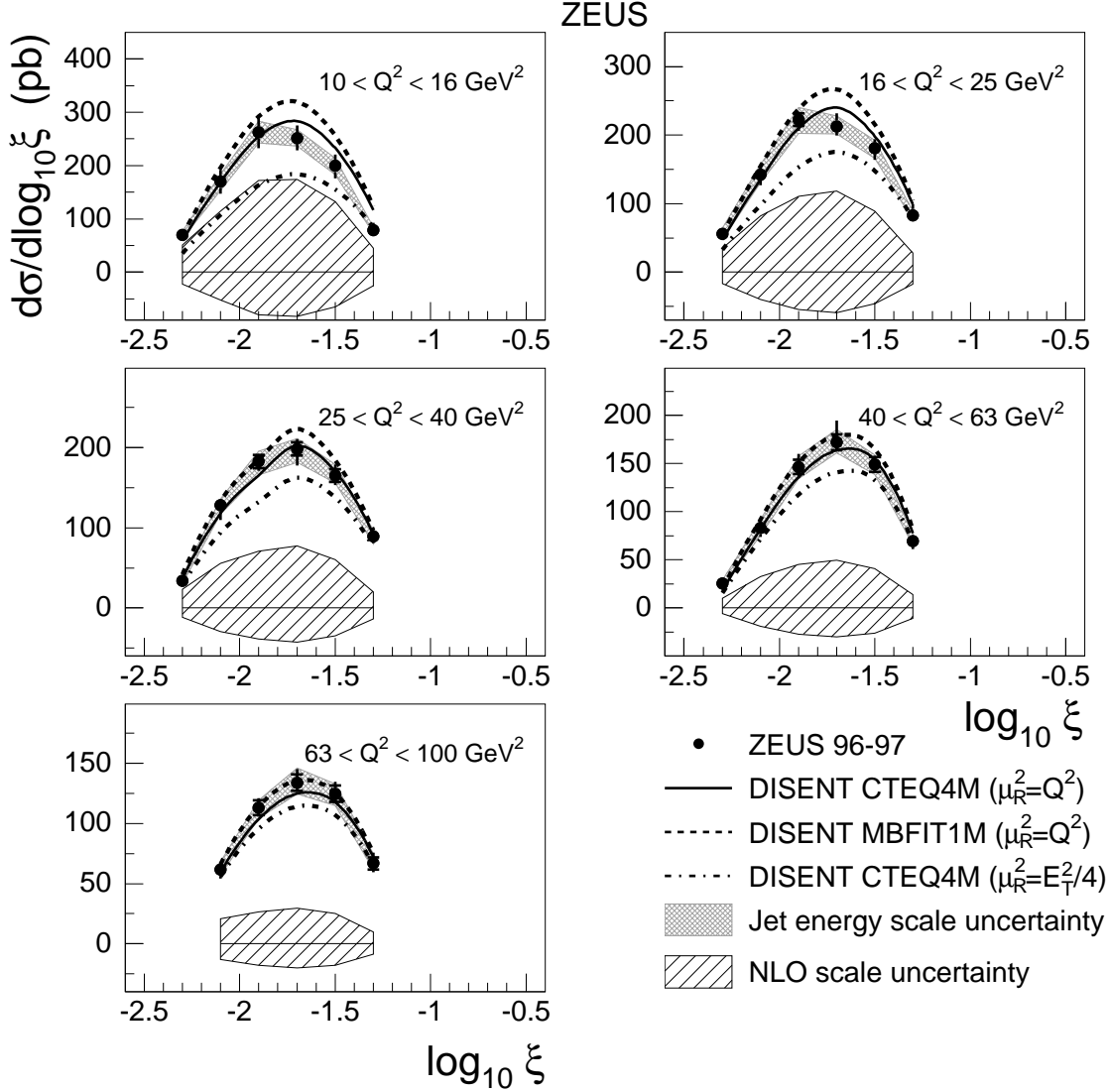


Figure 10: Dijet cross sections, $d\sigma/d \log_{10} \xi$, for jets of hadrons selected with the inclusive k_T jet algorithm in different regions of Q^2 . The points represent the measured cross sections. The inner error bars represent the statistical uncertainties and the outer bars are the statistical and the uncorrelated systematic uncertainties added in quadrature. The shaded band represents the systematic uncertainty due to the jet-energy scale. The full line represents the predictions of NLO QCD using DISENT with $\mu_R^2 = Q^2$ and the CTEQ4M proton PDFs. The dot-dashed line is the prediction of DISENT with $\mu_R^2 = E_T^2/4$ and the CTEQ4M proton PDFs. The dashed line is the prediction of DISENT with $\mu_R^2 = Q^2$ using the MBFIT1M proton PDFs. The cross-hatched band at the bottom of each plot is the μ_R^2 uncertainty calculated by varying μ_R^2 in the range $(4Q^2, Q^2/4)$. All of the pQCD predictions shown here refer to jets of hadrons and were obtained by dividing the parton level predictions of DISENT by the average value of the correction factors computed using the LEPTO 6.5 and the ARIADNE 4.10 MC simulations.

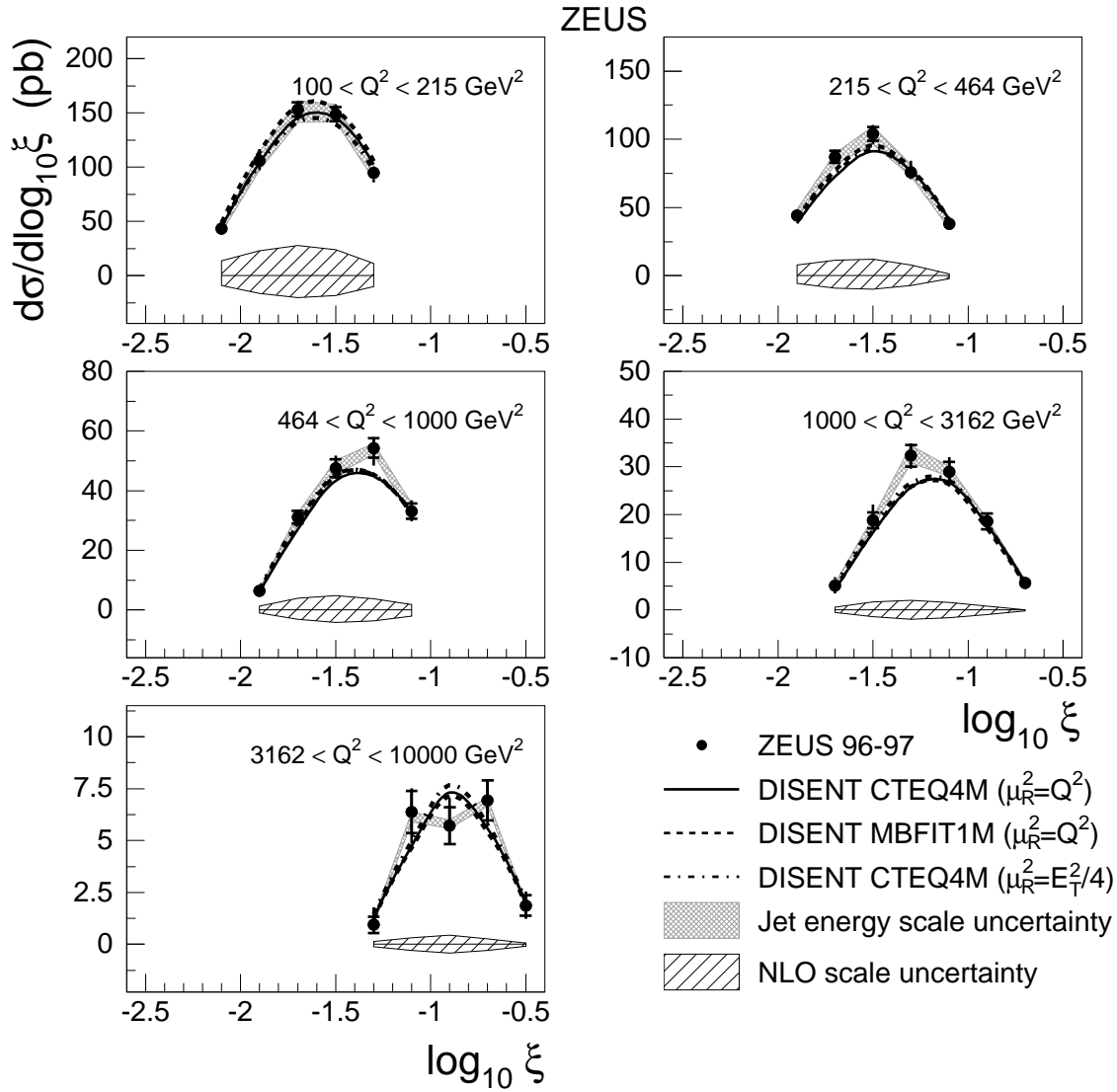


Figure 11: Continuation of Fig. 10 for higher values of Q^2 . Details are as described in the caption of Fig. 10.